

Simulating a slow bar in the low surface brightness galaxy UGC 628

Matthew H. Chequers,^{1*} Kristine Spekkens,^{1,2} Lawrence M. Widrow¹
and Colleen Gilhuly¹

¹*Department of Physics, Engineering Physics, and Astronomy, Queen's University, Kingston, ON K7L 3N6, Canada*

²*Department of Physics, Royal Military College of Canada, P.O. Box 17000, Station Forces, Kingston, ON K7L 7B4, Canada*

Accepted XXX. Received YYY; in original form ZZZ

ABSTRACT

We present a disc-halo N-body model of the low surface brightness galaxy UGC 628, one of the few systems that harbours a “slow” bar with a ratio of corotation radius to bar length of $\mathcal{R} \equiv R_c/a_b \sim 2$. We select our initial conditions using SDSS DR10 photometry, a physically motivated radially variable mass-to-light ratio profile, and rotation curve data from the literature. A global bar instability grows in our sub-maximal disc model, and the disc morphology and dynamics agree broadly with the photometry and kinematics of UGC 628 at times between peak bar strength and the onset of buckling. Prior to bar formation, the disc and halo contribute roughly equally to the potential in the galaxy’s inner region, giving the disc enough self gravity for bar modes to grow. After bar formation there is significant mass redistribution, creating a baryon dominated inner and dark matter dominated outer disc. This implies that, unlike most other low surface brightness galaxies, UGC 628 is not dark matter dominated everywhere. Our model nonetheless implies that UGC 628 falls on same the relationship between dark matter fraction and rotation velocity found for high surface brightness galaxies, and lends credence to the argument that the disc mass fraction measured at the location where its contribution to the potential peaks is not a reliable indicator of its dynamical importance at all radii.

Key words: galaxies: evolution – galaxies: individual: UGC 628 – galaxies: kinematics and dynamics

1 INTRODUCTION

Bars provide a testing ground for our theories of galaxy evolution, structure and dynamics. In particular, since the susceptibility of a galactic disc to bar-like instabilities is a function of the relative contributions to the gravitational potential of the disc, bulge, and dark halo, bars can be used to constrain mass models and break the disc-halo degeneracy that plagues rotation curve decomposition. The strength, pattern speed, and length of a bar all depend on the structure of the host galaxy, a point illustrated in numerous N-body experiments. For example, the quintessential strong, thin, and long bar can develop through an $m=2$ instability in galaxy models where the disc contribution to the centripetal force is comparable to that of the bulge and halo inside a few disc scale lengths (e.g see the review by Sellwood 2014). By contrast, if the disc completely dominates the centripetal force in the inner region, the bar that develops will be shorter, fatter,

and more boxy (Athanasoula 2003).

The contribution of the disc to the centripetal force can be represented by the dimensionless ratio

$$\mathcal{F}_X = V_d(XR_d)/V(XR_d), \quad (1)$$

where $V(R)$ is the total circular speed at radius R , V_d is the contribution to V from the disc, and X denotes a multiple of the exponential disc scale length R_d (van Albada et al. 1985; Sackett 1997). \mathcal{F}_X is commonly evaluated at $R = 2.2R_d$, where the disc contribution to the mass distribution peaks. It is often more useful to consider disc maximality in terms of \mathcal{F}_X^2 , rather than the classical quantity defined in equation (1), since \mathcal{F}_X^2 is a more direct measure of the mass contribution from the disc to the total mass budget of the galaxy enclosed within the radius XR_d . By convention, discs are described as maximal if $\mathcal{F}_{2.2}^2 > 0.72$. The first case described above corresponds to a submaximal disc ($\mathcal{F}_{2.2}^2 \approx 0.5$) while the second, a maximal one.

In this paper, we consider the low surface brightness

* E-mail: mchequers@astro.queensu.ca

(LSB) galaxy UGC 628. This galaxy has a clear photometric bar (de Blok et al. 2001; de Blok & Bosma 2002; Chemin & Hernandez 2009) and is commonly classified as Sbc–Sm (de Vaucouleurs et al. 1991). LSB galaxies are thought to be dark matter dominated in the inner disc (Bothun et al. 1997; de Blok & McGaugh 1997; de Blok et al. 2001; Combes 2002; de Blok & Bosma 2002; Kuzio de Naray et al. 2008) and indeed, the mass model for UGC 628 by de Blok & Bosma (2002) has $\mathcal{F}_{2.2}^2 \approx 0.09\text{--}0.16$. The mere presence of a bar in a galaxy with such a small $\mathcal{F}_{2.2}^2$ value already challenges our understanding of bar formation because self-gravity in the disc is so low (Mayer & Wadsley 2004). Indeed, the bar fraction in LSB galaxies is a mere $\sim 4\%$ (Mihos et al. 1997), while that in their high surface brightness counterparts is about an order of magnitude higher (e.g. Marinova & Jogee 2007).

Our main interest in UGC 628 is due to the claim by Chemin & Hernandez (2009) that its bar is “slow”. A bar with pattern speed Ω_p has a corotation resonance at radius R_c defined by the condition $\Omega(R_c) = V(R_c)/R_c = \Omega_p$. Corotation sets a theoretical upper bound on the length of the bar a_B and therefore the dimensionless ratio $\mathcal{R} \equiv R_c/a_B$ is expected to be greater than unity. Moreover, for a given a_B , $\Omega_p < \Omega(a_B)$ so long as Ω is a decreasing function of R , which is almost always the case. Thus, bars with \mathcal{R} close to unity have a pattern speed as fast as nature will allow. By convention, bars are defined respectively as “fast” or “slow” depending on whether \mathcal{R} is less than or greater than 1.4.

It is notoriously difficult to measure the length and pattern speed of bars in real galaxies (and for that matter, simulated ones) and therefore estimates of \mathcal{R} are generally plagued by large uncertainties. Nevertheless, of the tens of galaxies (Rautiainen et al. 2008; Aguerra et al. 2015) for which \mathcal{R} has now been measured, the vast majority appear to be fast. Indeed, UGC 628 is one of only three galaxies that are observed to have a slow bar, the others being the blue compact dwarf NGC 2915 (Bureau et al. 1999) and the dwarf irregular NGC 3741 (Banerjee et al. 2013).

The preponderance of fast bars especially among massive, bright galaxies is easy to understand. Once a bar-like perturbation develops, it causes circular orbits inside corotation to become elongated in the same sense as the perturbation thereby enhancing the putative bar. By contrast, circular orbits outside corotation are elongated perpendicular to the perturbation (See Contopoulos 1980). The bar rapidly develops and grows out to its corotation radius. The bar pattern speed may decrease with time, via dynamical friction (Chandrasekhar 1943; Mulder 1983; Weinberg 1985) for example, however, this only allows for more stars to participate in the bar mode as corotation is pushed to larger radii. Thus, Ω_p can decrease but the bar remains “fast” (Athanasoula 2013).

These arguments may not hold for LSB galaxies. Marinova & Jogee (2007) showed that a_B rarely exceeds R_{25} , the radius the surface brightness isophote equals $25 \text{ mag arcsec}^{-2}$. Evidently, once R_c approaches R_{25} discs lack the surface density out to corotation necessary to support a fast bar. Additionally, the strong shear in this region implied by flat galaxy rotation curves destabilizes the development of precessing bar orbits. Thus, it may not be surprising that an LSB galaxy (where the surface brightness is everywhere lower than in typical discs) like UGC 628 harbours one of the

few known examples of a slow bar.

The previous discussion suggests that \mathcal{R} should depend on a galaxy’s morphological type. This hypothesis is supported by Rautiainen et al. (2008) who estimated pattern speeds for 38 barred galaxies by modelling near-infrared and optical images. In short, they simulated the response of a gas and stellar disc to a rigidly rotating $m=2$ potential perturbation and varied Ω_p until the simulated disc morphologies matched observations. They found that \mathcal{R} gradually increased from early to late type galaxies; Sa through Sb galaxies tended to have fast bars while Sbc through Scd galaxies tended to have slow ones. By contrast, the bar pattern speeds measured by Aguerra et al. (2015), who applied the Tremaine–Weinberg method (Tremaine & Weinberg 1984) to stellar absorption line maps and optical images of 15 CALIFA survey galaxies, all point to fast bars with no dependence on morphology. However, they did not include galaxies with Hubble type later than Sbc. Thus, whether bars are generally fast or slow remains an open question.

In this paper, we present a dynamical N-body model for UGC 628 by evolving an (initially) exponential stellar disc in a live Navarro–Frenk–White (NFW) halo (Navarro et al. 1996) for ~ 12 Gyr. Our goals are two-fold. The first is to construct a model of this LSB galaxy that forms a bar. Indeed, the exponential disc inferred by de Blok & Bosma (2002) for UGC 628 has so little mass that, when evolved as an N-body model, it develops flocculent spiral structure but no bar. We re-examine the surface photometry of UGC 628 using updated multi-colour images and a variable stellar mass-to-light ratio. We find a steeper surface density profile than previously reported, from which we construct a bar-unstable N-body model that reproduces the morphology and kinematics of UGC 628 at late times. With this model in hand, we then proceed to examine how the bar in UGC 628 redistributes mass in the disc and the implications of that re-distribution for the dark matter mass fraction in this LSB galaxy.

Our procedure for constructing the dynamical model of UGC 628 is outlined in Section 2. This model provides initial conditions for our N-body simulations, which are described in Section 3 where we compare our model to observations of UGC 628 and discuss the quantitative properties of the bar. We discuss the implications of our results for the mass distribution in UGC 628 and summarize in Section 4. Throughout, we adopt a distance for UGC 628 of 71.2 Mpc and an inclination of 56° (Chemin & Hernandez 2009).

2 MODELLING UGC 628

In this section we present our approach for constructing N-body models of UGC 628. We derive the galaxy’s surface density profile from extant SDSS data and colour-mass-to-light ratio relations in Section 2.1 and use it together with rotation curve data described in Section 2.2 to generate initial conditions for the simulations detailed in Section 2.3.

2.1 Surface Density Profile from Photometry

Fig. 1 describes how we infer the surface density profile of UGC 628 from photometric data. The image processing suite

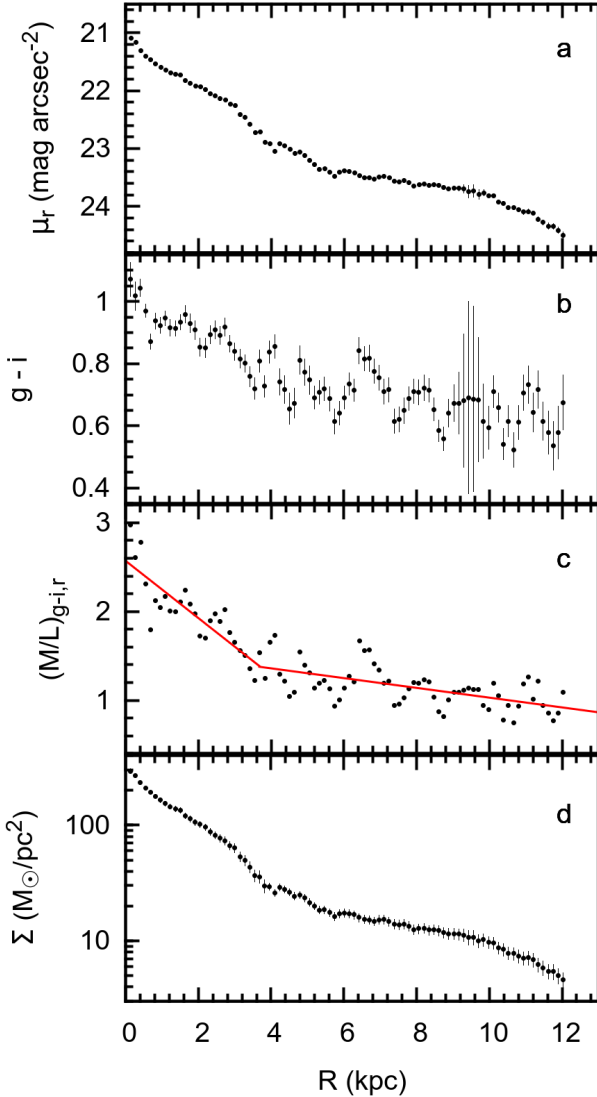


Figure 1. Derivation of the stellar surface density profile of UGC 628. Panel a: SDSS DR10 r -band surface brightness profile. Panel b: $g-i$ colour profile derived from the r -band isophotal solution. Panel c: Mass-to-light profile derived from the [Into & Portinari \(2013\)](#) ($g-i,r$) colour-band relation. The piecewise linear fit is shown as a solid red line. Panel d: Surface density profile produced by multiplying the surface brightness profile in panel a and the piecewise linear fit in panel c.

XVISTA¹ was used to fit isophotal contours to an SDSS DR10 ([Ahn et al. 2014](#)) r -band image. The break in the resulting r -band isophotal profile (Fig. 1a) at ~ 4 kpc divides the disc into two regions, with the inner region corresponding to the bar. The r -band solution was imposed on g - and i -band images and surface brightness profiles were generated in each band.

[Into & Portinari \(2013\)](#) tabulated colour-mass-to-light relations for a variety of bands, and mass-to-light profiles derived using different combinations of g , i , and r for UGC 628 are comparable. The $g-i$ colour profile presented in Fig. 1b was selected to take advantage of the colour stability due

¹ <http://ganymede.nmsu.edu/holtz/xvista>

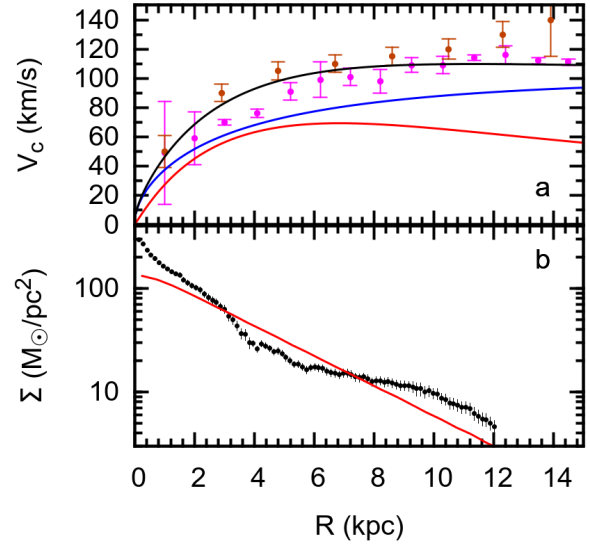


Figure 2. The rotation curve and surface density profile of the equilibrium initial conditions for our UGC 628 model. Panel a: Initial disc (red), halo (blue), and total (black) circular velocity curves for the model, and derived rotation curves from [de Blok & Bosma \(2002\)](#) (dark orange points) and [Chemin & Hernandez \(2009\)](#) (magenta points). Panel b: Initial surface density profile (black points) overplotted on the inferred UGC 628 profile (solid red line; see Section 2.1).

to the largest difference between bands. The $g-i$ colour profile shows a number of features with amplitudes ~ 0.2 mag and length scales of order 1 kpc. The most pronounced of these occur for R between 3 and 9 kpc and are likely due to colour variations in the bar and spiral arms. We note that the bar is also responsible for large, rapid variations in the ellipticity and position angle of the r -band isophotal contours, which were used to derive the g - and i -band surface brightness profiles. The inner portion of the resulting mass-to-light ratio profile, shown in Fig. 1c, has higher mass-to-light and a steeper gradient than the outer portion of the profile. Thus, we model the mass-to-light ratio profile as a continuous piecewise linear function with two segments.

Fig. 1d shows the inferred surface density profile that was constructed by combining the r -band surface brightness profile in Fig. 1a and the mass-to-light profile fit in Fig. 1c. The uncertainties were calculated by propagating uncertainty from the r -band surface brightness profile and the piecewise linear fit of the mass-to-light profile. This surface density profile guided the selection of initial disc parameters in the N-body simulations of UGC 628, and serves as a basis of comparison with simulation snapshots. In comparison, the surface density profile of the [de Blok & Bosma \(2002\)](#) model of UGC 628 possesses a shallower slope and much smaller central density, which results from measuring an exponential scale length in the outer part of the surface brightness profile ([de Blok et al. 1995](#)) and applying a constant mass-to-light ratio.

2.2 Rotation Curve Data

Rotation curve data derived from optical $H\alpha$ velocity field observations from [de Blok & Bosma \(2002\)](#) and [Chemin &](#)

Table 1. Initial galaxy model parameters. The first block corresponds to parameters used to build the initial equilibrium N-body models using the GalactICS code (Kuijken & Dubinski 1995; Widrow et al. 2008). The second block corresponds to parameters derived from values in the first block.

Parameter	Our Model	de Blok & Bosma (2002)
M_d [$10^9 M_\odot$] ^a	9.239	5.882
R_d [kpc] ^b	2.909	4.7
z_d [kpc] ^c	0.485	0.783
R_{out} [kpc] ^d	25	25
σ_0 [km s ⁻¹] ^e	31.7	10.4
R_σ [kpc] ^f	2.909	4.7
a_h [kpc] ^g	14	10.8
σ_h [km s ⁻¹] ^h	210.0	262.5
r_{200} [kpc] ⁱ	112	130
$Q(2.5R_d)$ ^j	1	1
M_{200} [$10^{11} M_\odot$] ^k	1.843	2.807
c ^l	8	12
$\mathcal{F}_{2.2}^2$ ^m	0.44	0.13

Disc mass^a; radial disc scale length^b; vertical disc scale height^c; outer disc truncation radius^d; central radial velocity dispersion in the disc^e; radial scale length of the radial velocity dispersion profile in the disc^f; NFW halo scale length^g; central velocity dispersion of the halo^h; outer radius of the haloⁱ; Toomre Q parameter at $2.5R_d$ ^j; halo mass^k; halo concentration^l; disc mass contribution to the total galaxy mass within $2.2R_d$ ^m.

Hernandez (2009) is shown in Fig. 2a. We see that the two data sets are formally inconsistent with one another, particularly in the range $R \sim 3$ -6 kpc. This discrepancy in the inner region is mitigated when improved H α velocity field data with higher angular sampling, compared to Chemin & Hernandez (2009), are considered (L. Chemin, private communication). However, we note that neither Chemin & Hernandez (2009) nor de Blok & Bosma (2002) accounted for bisymmetric flows when deriving rotation curves from the measured line-of-sight velocities. Because the bar in UGC 628 projects near the major axis, rotation curves derived ignoring the bar flows are biased low relative to the true circular velocity (Spekkens & Sellwood 2007; Dicaire et al. 2008; Randriamampandry et al. 2016). We account for this observational bias when comparing our models to the rotation curve data sets in Section 3.1. We do use the general shape of the rotation curve, especially in the outer regions of the galaxy where $V(R)$ is approximately constant, to guide the selection of halo model parameters.

2.3 Initial Conditions for N-body Simulations

We generate initial conditions for our N-body simulations using the GalactICS code (Kuijken & Dubinski 1995; Widrow et al. 2008), which allows one to construct axisymmetric, multicomponent galaxy models that are in approximate dynamical equilibrium. The models in the present study comprise a stellar disc and an NFW dark halo. Particles for the disc are drawn from a phase space distribution function that depends on the energy, angular momentum about the symmetry axis, and vertical energy. By construction, this distribution function yields a disc whose space density is given by

$$\rho_d(R, z) = \frac{M_d}{4\pi R_d^2 z_d} e^{-R/R_d} \text{sech}^2(z/z_d), \quad (2)$$

where M_d is the total disc mass and z_d is the disc scale height. In addition, the radial velocity dispersion of the disc is an exponential function of R :

$$\sigma_R(R) = \sigma_0 e^{-R/2R_\sigma}, \quad (3)$$

where σ_0 is the central dispersion and R_σ is the radial scale length of the squared dispersion profile. The velocity dispersion in the azimuthal direction is calculated from the epicycle approximation. Finally, the disc is constructed to be approximately isothermal in the direction perpendicular to the disc plane.

The halo distribution function depends only on the energy and is constructed to yield an NFW density profile (Navarro et al. 1996)

$$\rho_h(r) = \frac{a_h \sigma_h^2}{4\pi G} \frac{1}{r(r+a_h)^2}, \quad (4)$$

where a_h is the NFW scale length and σ_h is the characteristic velocity scale.

The input values for R_d and M_d are found by fitting the surface density profile to a single exponential function, as shown in Fig. 2b. We then set $z_d = R_d/6$ as suggested in a study of edge-on galaxies by van der Kruit & Searle (1981). Furthermore, we assume that the exponential scale length for σ_R^2 is the same as for the surface density, i.e. $R_\sigma = R_d$ (Bottema 1993). Finally, we set the central radial velocity dispersion so that the Toomre Q parameter (Toomre 1964) is equal to unity at $R = 2.5R_d$.

The halo parameters a_h and σ_h were chosen to produce a reasonable fit (chi-by-eye) to the observed outer rotation curve. A comparison of the disc-halo rotation curve decomposition of our initial conditions and the de Blok & Bosma (2002) and Chemin & Hernandez (2009) data is shown in Fig. 2a. If we define the total mass in dark matter by the standard M_{200} (mass interior to radius r_{200} , which is defined as the radius inside which the mean density is 200 times the critical density), then our model has a disc mass fraction of $f_d = M_d/M_{200} = 0.05$ and a halo concentration $c = 8$. As noted by Mayer & Wadsley (2004), LSB galaxies typically have mass fractions $f_d \leq 0.1$ and can be bar unstable with halo concentrations as low as $c = 4$.

Parameter values used for our model are presented in Table 1. The disc and halo distribution functions were populated with 10^6 and 2×10^6 particles, respectively. The models were simulated using GADGET-2 (Springel 2005) for ~ 11.7 Gyr (roughly 195 dynamical times at $R = 2.2R_d$) with a softening length of 40 pc for both disc and halo particles. Minimum and maximum time steps were set to 0.01% and 0.2% of the galactic dynamical time defined at a radius of 20 kpc. Energy was conserved to within a maximum of 0.04% over the simulation runtime.

Additional simulations were run to test the sensitivity of our results to the model parameters; and we have verified that models with initial parameter values of $2 < R_d < 3.5$ kpc and $1 < Q(2.5R_d) < 1.5$ produce similar results. The same cannot be said for an N-body model with the shallower, less

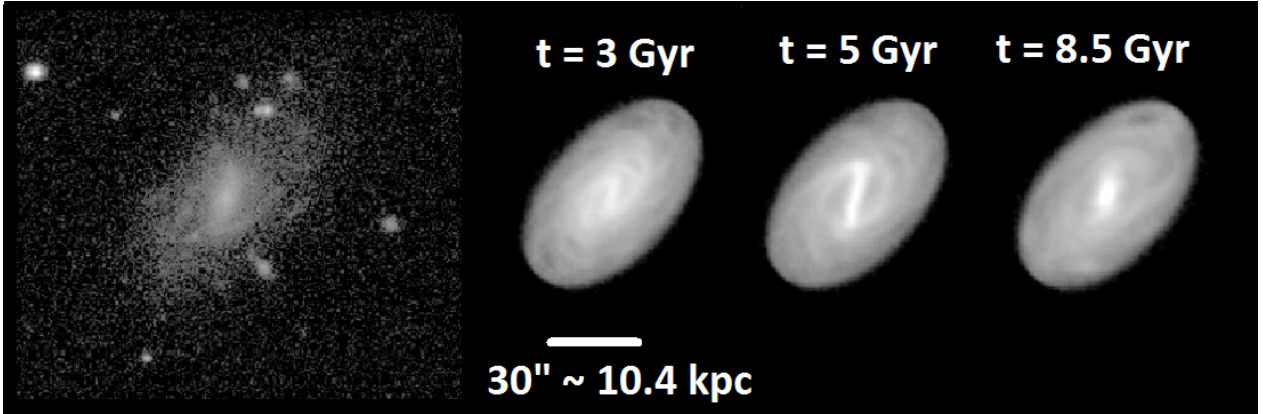


Figure 3. The surface brightness distributions of our UGC 628 model when the bar mode begins to grow ($t = 3$ Gyr), at peak bar strength ($t = 5$ Gyr), and after buckling ($t = 8.5$ Gyr), projected on the sky plane using the same log-scale. The leftmost image is a sky-subtracted log-scale r -band SDSS image of UGC 628. A distance legend corresponding to both the simulated and observed images is also shown.

dense disc of [de Blok & Bosma \(2002\)](#). The parameters for our realization of their model are also given in Table 1. In this case, the galaxy develops flocculent spiral structure but never forms a bar.

3 BAR FORMATION AND EVOLUTION IN THE SIMULATED MODELS

3.1 Comparison to UGC 628

In Fig. 3 we show a sky subtracted log-scale r -band image of UGC 628 alongside the projected log-scale disc surface brightness from our simulation when the bar mode begins to grow ($t = 3$ Gyr), at peak bar strength ($t = 5$ Gyr), and after buckling ($t = 8.5$ Gyr; see Section 3.2). The surface brightness images were constructed by applying the mass-to-light fit (Fig. 1c) to convert N-body particle mass to luminosity. The bar position angle in the simulations was chosen to match that in the observations. Additionally, the simulated discs were truncated at $R = 12.5$ kpc before they were projected onto the sky to mimic the sky subtraction used in producing the r -band image.

At all times, the inner disc of our model has a clear central bar. In addition, spiral arms emanating from the ends of the bar are visible, especially in the $t = 3$ and $t = 5$ Gyr snapshots. The bar at 5 Gyr is far narrower than that in the r -band image. Conversely, the bar at 8.5 Gyr does not extend quite as far in length as the bar in UGC 628. Thus, the bar in UGC 628 may be best-fit by our model at a time between peak strength and buckling.

The surface density and rotation curve decomposition profiles at $t = 3, 5,$ and 8.5 Gyr are presented in Fig. 4. The evolution of the surface density profile in the top row of Fig. 4 shows considerable mass redistribution within the disc. Disc material initially at $R \sim 5$ kpc is mainly redistributed to the central bar region, although some disc material moves to the outer disc near R_c . We note that, even just after the formation of the bar at $t = 3$ Gyr, the disc surface density at R_c is low and the shear is high because the rotation curve is already flat.

The surface density profile at $t = 8.5$ Gyr matches the

observed profile decently, and the break in the profile occurs around the correct radius. Additionally, the surface density in the outer disc captures the proper decrease in density apparent in the observational data. Of course, choosing to compare the surface density profile at $t = 8.5$ Gyr to observations is arbitrary, and we find slightly better or worse agreement depending on the simulation snapshot. However, after the bar buckles the surface density stays roughly constant while the disc is continually being heated in both the in-plane and vertical directions.

The circular velocity curves in the bottom row of Fig. 4 were computed by calculating the total in-plane force from all particles (black line) and from the disc (red line) and halo (blue line) potentials using direct summation on 5000 test particles uniformly distributed within the disc mid-plane. For $R > 5$ kpc, the model rotation curves are in good agreement with the observed rotation curves at all times. At later times once the bar has buckled, the disc contribution in the bar region is strongly increased. For $R < 5$ kpc, the initial circular velocity is considerably larger than that measured by [Chemin & Hernandez \(2009\)](#), but agrees with that obtained by [de Blok & Bosma \(2002\)](#). The increased circular velocity of the system at later times in the simulation is also broadly consistent with the [de Blok & Bosma \(2002\)](#) measurements except at $R = 1$ kpc, where the simulated circular velocity exceeds the measured value. As discussed above, this discrepancy between our model and the data is not surprising because [Chemin & Hernandez \(2009\)](#) and [de Blok & Bosma \(2002\)](#) do not account for bisymmetric flows when deriving the rotation curves (see Section 2.2). The cyan lines in the bottom panels of Fig. 4 show the rotation curves that we derive from line-of-sight velocities of the model projections in Fig. 3, under the assumption of axisymmetry. There is good agreement between these curves and the observational data.

3.2 Bar Properties

Section 3.1 established good qualitative agreement between the photometry and kinematics of UGC 628 and those of our barred galaxy model around the time of buckling. To

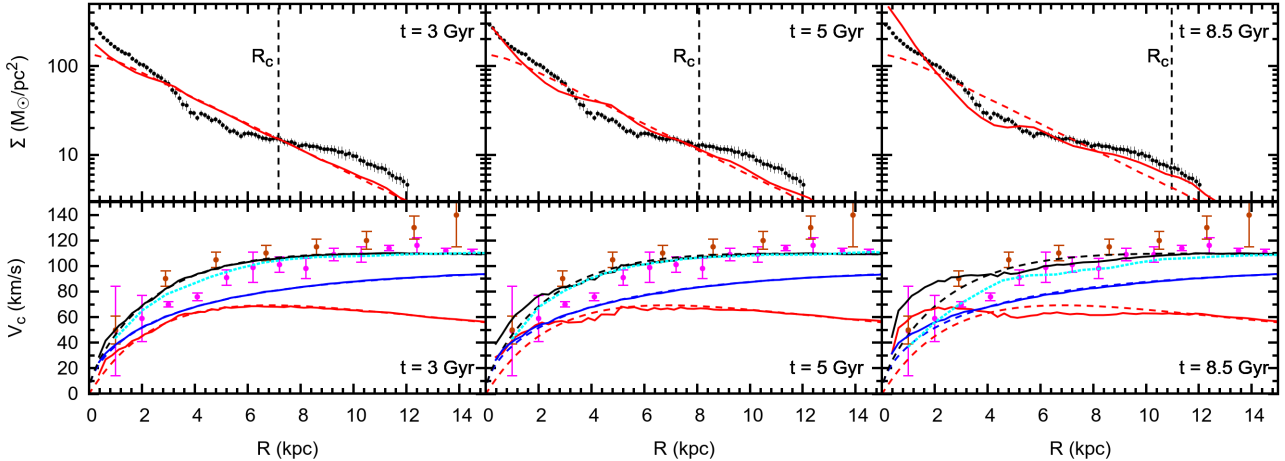


Figure 4. Evolution of the mass distribution and rotation curve in our model of UGC 628. Columns correspond to various times in the simulation as indicated. Top row: Surface density profile. The observed surface density profile is shown as black points, the initial conditions of the model are shown as a red dashed line, and the surface density profile of the model at the indicated time is shown as a solid red line. Only uncertainties larger than the data points are shown. Vertical black dashed lines indicate the radius of corotation at each time. Bottom row: Circular rotation curve. The red, blue, and black lines correspond to the disc, halo, and total rotation curves, respectively. The model initial conditions correspond to the dashed lines, while the solid lines show the rotation curve at the time indicated. Observational data from [de Blok & Bosma \(2002\)](#) and [Chemin & Hernandez \(2009\)](#) are shown as dark orange and magenta points, respectively. The cyan line shows the rotation curve derived from the line-of-sight velocities for the model projections shown in [Fig. 3](#), under the assumption of axisymmetry, for comparison with the observational data.

quantify the strength of the bar modes in our model we expand the surface density of the disc into a Fourier series in azimuthal angle ϕ of m -fold density symmetries and find the magnitude of the $m=2$ Fourier coefficient ([Sellwood & Athanassoula 1986](#)) for all disc particles with cylindrical radius $R < 5$ kpc, the region that encompasses the bar at late times. We assume that the bar is the only bisymmetric mode present for $R < 5$ kpc at all times, and that contamination from bisymmetric spiral modes is limited. We define the Fourier coefficient for the m th mode at time t as

$$A_m(t) = \frac{1}{N} \sum_{j=1}^N e^{im\phi_j}, \quad (5)$$

where N is the number of particles with $R < 5$ kpc, $m=2$ for a bisymmetric bar mode, and ϕ_j is the azimuthal position of the j th particle. We define the bar strength as the magnitude of equation (5).

The bar strength as a function of time for our model is shown in [Fig. 5a](#). After buckling, the bar settles in strength for the remainder of the simulation. In comparison, the bisymmetric mode strength in the constant mass-to-light [de Blok & Bosma \(2002\)](#) model remained at the initial noise level of $|A_2| \sim 10^{-2}$ over the entire simulation runtime, which is more than an order of magnitude smaller than the bar strength measured in any of the variable mass-to-light models that we simulated.

To compute the bar pattern speed Ω_p , we evaluate the numerical derivative of the cumulative azimuthal phase of the $m=2$ density mode in the inner disc ([Ridders 1982](#); [Press et al. 2007](#)). The result is presented in [Fig. 5b](#) and is generally consistent with measurements by [Chemin & Hernandez \(2009\)](#) over the lifetime of the bar, particularly after the time of peak strength at $t \sim 5$ Gyr. The pattern speed be-

gins to decrease once the bar reaches maximum strength, presumably due to dynamical friction from the halo ([Chandrasekhar 1943](#); [Mulder 1983](#); [Weinberg 1985](#)). At the onset of bar buckling ($t \sim 7$ Gyr) the rate at which the pattern speed decreases changes and stays constant for the remainder of the simulation.

To quantify the relative speed of the bar we compute \mathcal{R} as a function of time. The radius at which $\Omega(R) = \Omega_p$ in [Fig. 5b](#) defines R_c . Accurate and robust determination of bar lengths in simulations is a long standing challenge ([Micheldansac & Wozniak 2006](#)). We estimate the bar semi-major axis using a method similar to that described in [Debattista & Sellwood \(2000\)](#), where a_B is defined as the location of the upturn in the radial profile of $|A_2|$ near the bar edge. As noted by [Debattista & Sellwood \(2000\)](#), this method tends to underestimate the length of the bar, particularly in the presence of noise. We mitigate this effect by considering the weighted mean of \mathcal{R} over a dynamical time, where outlying values are down-weighted.

The resulting values of \mathcal{R} are shown in [Fig. 5c](#), and fall within the confidence bounds of measurements by [Chemin & Hernandez \(2009\)](#) for most of the simulation once the bar has formed, and especially at later times after the bar has begun to buckle. The large variability in \mathcal{R} relative to Ω_p and $|A_2|$ ([Fig. 5a,b](#)) arises because it is a ratio of two noisy quantities, R_c and a_B , particularly for $t < 5$ Gyr when the bar is still growing. It is clear that the bar in our model is slow, with $\mathcal{R} > 1.4$ over the entire bar lifetime. We note that both R_c and a_B do increase over time, however, a_B does so at a lesser rate and would have to approximately double in value for the bar to be considered “fast”.

A more visual depiction of the bar’s relative speed is shown in [Fig. 6](#), where the power spectrum of bisymmetric mode frequencies is plotted as a function of radius for

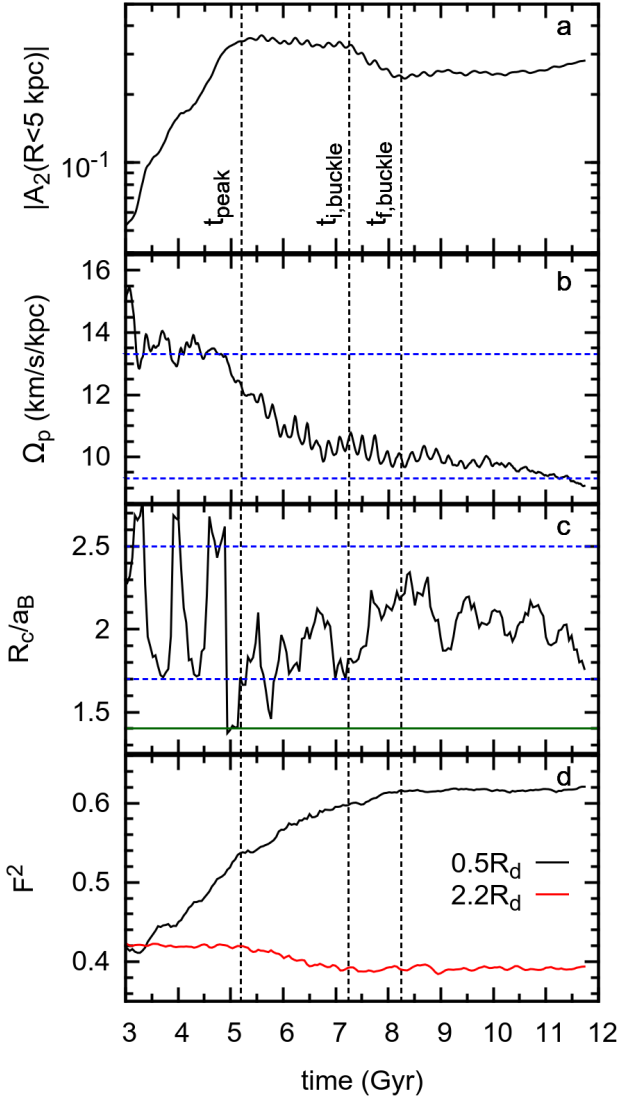


Figure 5. Quantitative properties of the bar and disc as a function of time for the UGC 628 model. All quantities are averaged over a galactic dynamical time defined at a radius of 20 kpc. Vertical black dashed lines indicate times of peak strength, start of buckling, and the end of buckling, as labelled. Panel a: Bar strength. Panel b: Bar pattern speed. The range of measured values allowed by the 1σ uncertainties of Chemin & Hernandez (2009) is indicated as horizontal blue dashed lines. Panel c: Ratio of corotation radius and bar semi-major axis length. The range of measured values allowed by the 1σ uncertainties of Chemin & Hernandez (2009) are indicated as horizontal blue dashed lines. The horizontal solid green line indicates the cut-off between fast and slow bars, $\mathcal{R} = 1.4$. Panel d: Disk mass fraction. The black and red lines correspond to measurements evaluated at $0.5R_d$ and $2.2R_d$, respectively.

$5 < t < 8.5$ Gyr (Sellwood & Athanassoula 1986; Press et al. 2007, see also Roškar et al. (2012) for a succinct description). The epicyclic frequency used to compute resonant frequencies in Fig. 6 was calculated from

$$\kappa^2 = 4\Omega^2(R) + R \frac{d}{dR} \Omega^2(R), \quad (6)$$

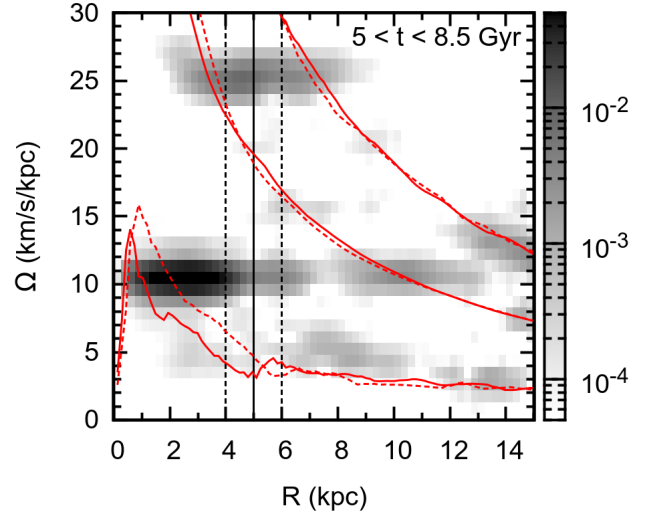


Figure 6. Power spectrum of $m=2$ density mode frequencies in the simulated model as a function of cylindrical radius for $5 < t < 8.5$ Gyr. The vertical black lines correspond to the average measurement of a_B over the specified time frame (solid) and the associated 1σ uncertainty (dashed). The red lines show the inner Lindblad, corotation, and outer Lindblad resonances (from left to right) at $t = 5$ Gyr (solid) and 8.5 Gyr (dashed).

where $\Omega(R) = V(R)/R$ is the circular frequency profile of the galaxy and $V(R)$ is the circular speed computed from the in-plane forces, as described in Section 3.1 (Binney & Tremaine 2008). The peak in power at $(R, \Omega) \sim (3 \text{ kpc}, 10 \text{ km s}^{-1} \text{ kpc}^{-1})$ corresponds to the bar. The structure at $\Omega \sim 25 \text{ km s}^{-1} \text{ kpc}^{-1}$ between corotation and the outer Lindblad resonance corresponds to a bisymmetric spiral mode emanating from the edge of the bar. Also present in Fig. 6 are bisymmetric density modes that have accumulated along various resonances. The bar structure clearly does not extend to corotation, which is apparent from the order of magnitude difference in power between the peak power at $R \sim 3$ kpc and the structure closer to corotation along $\Omega \sim 10 \text{ km s}^{-1} \text{ kpc}^{-1}$. Thus, the bar is slow since it is rotating at a frequency far less than $\Omega(a_B)$.

To investigate how the relative disc and halo mass distributions change as a function of time we compute \mathcal{F}^2 , from equation (1), as a function of time evaluated at various multiples of the disc radial scale length of an exponential fit to the radial surface density profile for $R < 12$ kpc (Press et al. 2007). Fig. 5d shows $\mathcal{F}_{0.5}^2$ and $\mathcal{F}_{2.2}^2$ as a function of time, which serves as proxies for the mass contribution of the disc within $R = 0.5R_d$ and $R = 2.2R_d$, respectively. When the bar starts to form, $\mathcal{F}_{0.5}^2 \sim \mathcal{F}_{2.2}^2 \sim 0.4$. By the time the bar reaches peak strength there are equal mass fractions between the disc and halo in the bar region. The disc mass contribution steadily increases over time in the inner region and slightly decreases within $R = 2.2R_d$ until the bar buckles. After buckling, the relative fraction of disc and halo mass remains roughly constant in time with $\mathcal{F}_{0.5}^2 \sim 0.6$ and $\mathcal{F}_{2.2}^2 \sim 0.4$. Thus, between the times of peak bar strength and on the onset of buckling, when the model best corresponds to the photometry and kinematics of UGC 628, the model is baryon dominated in the bar region and dark matter dominated farther out.

4 DISCUSSION AND SUMMARY

We have presented N-body models of the barred LSB galaxy UGC 628, one of the few systems for which a slow ($\mathcal{R} = R_c/a_B > 1.4$) bar has been measured (Chemin & Hernandez 2009). We re-examined the surface brightness profile of UGC 628 by fitting SDSS DR10 photometry and applying the colour-mass-to-light ratio transformations of Into & Portinari (2013), finding a higher surface density than previously reported (de Blok & Bosma 2002). We used this surface density distribution together with rotation curve data from the literature to initialize our simulations with an exponential stellar disc with a fractional mass contribution enclosed within $R = 2.2R_d$ of $\mathcal{F}_{2.2}^2 = 0.44$ embedded in an NFW halo. The disc developed a bar that begins to grow at $t = 3$ Gyr, peaks in strength at $t = 5$ Gyr, and finishes buckling by $t = 8.5$ Gyr.

The model provides a good description of the available photometry and kinematics of UGC 628 at relatively late times, between the bar’s peak strength and buckling. The bar length and pattern speed that we measure from the simulations imply $\mathcal{R} \sim 2$ after the bar reaches peak strength, in broad agreement with the measurements of Chemin & Hernandez (2009). We find that the bar redistributes mass effectively in the inner disc; our model therefore implies that UGC 628 is baryon dominated in the bar region and dark matter dominated further out.

The observations for UGC 628 by Chemin & Hernandez (2009) and the models presented in this paper imply that, in agreement with the photometric models of Rautiainen et al. (2008), at least some late-type galaxies host slow bars. The pattern speed evolution of the bar in our model is broadly consistent with theoretical considerations and N-body simulations of submaximal discs, where drag from dynamical friction decreases the pattern speed (see Sellwood 2014, for a review). However, the bars in most simulations are “born fast” with $\mathcal{R} \sim 1$ just after they form (e.g. Debattista & Sellwood 2000), while $\mathcal{R} \sim 2$ in our model at all times. We attribute this difference to the relatively low stellar surface density and high shear in our model at $R = R_c$, which follow from the LSB classification and flat rotation curve of UGC 628, even at early times (Fig. 4): the disc therefore does not have sufficient self-gravity to support a bar mode out to corotation even before any braking has taken place.

Our model has a disc mass fraction within 2.2 exponential scale lengths of $\mathcal{F}_{2.2}^2 \sim 0.4$ throughout the simulation (Fig. 5d), and is therefore dark matter dominated according to that definition. With $V_{tot} = 110 \text{ km s}^{-1}$ and $f_{DM} = 1 - \mathcal{F}_{2.2}^2 \sim 0.6$, our model sits on the lower 1σ envelope of the universal relation proposed by Courteau & Dutton (2015), commensurate with LSB galaxies having systematically larger discs than their high surface brightness counterparts (e.g. Zwaan et al. 1995). Contrary to the conclusion of Chemin & Hernandez (2009) given the low pattern speed of the bar, however, our model suggests that UGC 628 is not dark matter dominated at all radii but instead has $\mathcal{F}_{0.5}^2 \sim 0.6$ at the onset of bar buckling. Thus our model of UGC 628 provides an example of the fact that, as argued by many authors in the past (Debattista & Sellwood 2000; Courteau & Dutton 2015), the disc mass fraction enclosed within the radius where its contribution peaks is not a reliable indicator of its dynamical importance at all radii. Pairing $\mathcal{F}_{2.2}^2$ with

a measure at smaller radii, such as $\mathcal{F}_{0.5}^2$, may be more informative (Fig. 5d), although the latter is even harder to constrain observationally than the former due to uncertainties in stellar population models, dust obscuration corrections, and bulge contributions near galaxy centres, particularly in more massive systems than the one considered here.

We note that simulations show that the presence of gas during bar growth and evolution can influence its final properties (e.g. Bournaud et al. 2005; Villa-Vargas et al. 2010; Athanassoula et al. 2013; Athanassoula 2014, but see Sellwood & Debattista 2014). Most of these simulations distribute the gas identically to the stars at the outset, and therefore reflect the influence of molecular gas discs rather than the more extended atomic gas ones (e.g. Broeils & Rhee 1997; Frank et al. 2016). The low star formation efficiency and quiescent star formation history of UGC 628 (Young et al. 2015) suggest a low molecular-to-atomic gas ratio both now and in the past, consistent with CO non-detections in late-type LSB galaxies (Das et al. 2006). In addition, UGC 628 itself has an unusually low atomic-to-stellar mass ratio of $M_{HI}/M_* \sim 0.2$ for an LSB galaxy (Springob et al. 2005; Kim 2007). We therefore expect the molecular gas fraction in UGC 628 to be low and its inclusion in our models to have little influence on the bar properties that we report here (Berentzen et al. 2007).

The baryon dominated central regions of UGC 628 implied by our model distinguish it from most other LSB galaxies, where kinematics and photometry suggest a dark matter dominated inner disc (Bothun et al. 1997; de Blok & McGaugh 1997; de Blok et al. 2001; Combes 2002; de Blok & Bosma 2002; Kuzio de Naray et al. 2008). The disc in UGC 628 therefore has enough self-gravity to support a bar but also a sufficiently low central surface brightness ($\mu_{B,0} = 23.1 \text{ mag arcsec}^{-2}$, Kim 2007) for the system to be classified as an LSB. Indeed, the rarity of bars in LSB galaxies (Mihos et al. 1997) suggests that this balance is a delicate one. It may be the case that the properties of the bar and mass distribution in UGC 628 found here also apply to the few other known barred LSB galaxies, though to our knowledge pattern speeds for these systems have not been measured. Estimates of \mathcal{R} and detailed dynamical models for these LSB galaxies as well as the other known systems with slow bars (Bureau et al. 1999; Banerjee et al. 2013) may help further explore the properties of such instabilities in late-type, low-mass, and LSB discs.

ACKNOWLEDGEMENTS

We would like to thank the anonymous referee for providing suggestions that improved the quality of this paper, E. Athanassoula for useful conversations, L. Chemin for generously providing data for a graduate class project from which this study emerged, and N. Deg for the algorithm used to produce sky projections of the simulated model in Fig. 3. We also acknowledge the use of computational resources at the Centre for Advanced Computing. MHC acknowledges the financial support of the Ontario Graduate Scholarship, Queen Elizabeth II Graduate Scholarship in Science and Technology, and Natural Sciences and Engineering Research Council Postgraduate Scholarship programmes throughout the duration of this work. KS and LMW are supported by

the Natural Sciences and Engineering Research Council of Canada through Discovery Grants. We acknowledge the use of data from SDSS-III. Funding for SDSS-III has been provided by the Alfred P. Sloan Foundation, the Participating Institutions, the National Science Foundation, and the U.S. Department of Energy Office of Science.

REFERENCES

Aguerri J. A. L., et al., 2015, *A&A*, **576**, A102
 Ahn C. P., et al., 2014, *ApJS*, **211**, 17
 Athanassoula E., 2003, *MNRAS*, **341**, 1179
 Athanassoula E., 2013, Bars and secular evolution in disk galaxies: Theoretical input. p. 305
 Athanassoula E., 2014, *MNRAS*, **438**, L81
 Athanassoula E., Machado R. E. G., Rodionov S. A., 2013, *MNRAS*, **429**, 1949
 Banerjee A., Patra N. N., Chengalur J. N., Begum A., 2013, *MNRAS*, **434**, 1257
 Berentzen I., Shlosman I., Martinez-Valpuesta I., Heller C. H., 2007, *ApJ*, **666**, 189
 Binney J., Tremaine S., 2008, *Galactic Dynamics: Second Edition*. Princeton University Press
 Bothun G., Impey C., McGaugh S., 1997, *PASP*, **109**, 745
 Bottema R., 1993, *A&A*, **275**, 16
 Bournaud F., Combes F., Semelin B., 2005, *MNRAS*, **364**, L18
 Broeils A. H., Rhee M.-H., 1997, *A&A*, **324**, 877
 Bureau M., Freeman K. C., Pfizner D. W., Meurer G. R., 1999, *AJ*, **118**, 2158
 Chandrasekhar S., 1943, *ApJ*, **97**, 255
 Chemin L., Hernandez O., 2009, *A&A*, **499**, L25
 Combes F., 2002, *New Astron. Rev.*, **46**, 755
 Contopoulos G., 1980, *A&A*, **81**, 198
 Courteau S., Dutton A. A., 2015, *ApJ*, **801**, L20
 Das M., O’Neil K., Vogel S. N., McGaugh S., 2006, *ApJ*, **651**, 853
 de Blok W. J. G., Bosma A., 2002, *A&A*, **385**, 816
 de Blok W. J. G., McGaugh S. S., 1997, *MNRAS*, **290**, 533
 de Blok W. J. G., van der Hulst J. M., Bothun G. D., 1995, *MNRAS*, **274**, 235
 de Blok W. J. G., McGaugh S. S., Bosma A., Rubin V. C., 2001, *ApJ*, **552**, L23
 de Vaucouleurs G., de Vaucouleurs A., Corwin Jr. H. G., Buta R. J., Paturel G., Fouqué P., 1991, *Third Reference Catalogue of Bright Galaxies*. Volume I: Explanations and references. Volume II: Data for galaxies between 0^h and 12^h . Volume III: Data for galaxies between 12^h and 24^h .
 Debattista V. P., Sellwood J. A., 2000, *ApJ*, **543**, 704
 Dicaire I., et al., 2008, *MNRAS*, **385**, 553
 Frank B. S., de Blok W. J. G., Walter F., Leroy A., Carignan C., 2016, *AJ*, **151**, 94
 Into T., Portinari L., 2013, *MNRAS*, **430**, 2715
 Kim J. H., 2007, PhD thesis, University of Maryland, College Park
 Kuijken K., Dubinski J., 1995, *MNRAS*, **277**, 1341
 Kuzio de Naray R., McGaugh S. S., de Blok W. J. G., 2008, *ApJ*, **676**, 920
 Marinova I., Jøgee S., 2007, *ApJ*, **659**, 1176
 Mayer L., Wadsley J., 2004, *MNRAS*, **347**, 277
 Michel-Dansac L., Wozniak H., 2006, *A&A*, **452**, 97
 Mihos J. C., McGaugh S. S., de Blok W. J. G., 1997, *ApJ*, **477**, L79
 Mulder W. A., 1983, *A&A*, **117**, 9
 Navarro J. F., Frenk C. S., White S. D. M., 1996, *ApJ*, **462**, 563
 Press W. H., Teukolsky S. A., Vetterling W. T., Flannery B. P., 2007, *Numerical Recipes. The Art of Scientific Computing*, 3rd edn. Cambridge University Press

Randriamampandry T. H., Deg N., Carignan C., Combes F., Spekkens K., 2016, preprint, ([arXiv:1608.00690](https://arxiv.org/abs/1608.00690))
 Rautiainen P., Salo H., Laurikainen E., 2008, *MNRAS*, **388**, 1803
 Ridders C., 1982, *Adv. Eng. Softw.*, **4**, 75
 Roškar R., Debattista V. P., Quinn T. R., Wadsley J., 2012, *MNRAS*, **426**, 2089
 Sackett P. D., 1997, *ApJ*, **483**, 103
 Sellwood J. A., 2014, *Reviews of Modern Physics*, **86**, 1
 Sellwood J. A., Athanassoula E., 1986, *MNRAS*, **221**, 195
 Sellwood J. A., Debattista V. P., 2014, preprint, ([arXiv:1410.0834](https://arxiv.org/abs/1410.0834))
 Spekkens K., Sellwood J. A., 2007, *ApJ*, **664**, 204
 Springel V., 2005, *MNRAS*, **364**, 1105
 Springob C. M., Haynes M. P., Giovanelli R., Kent B. R., 2005, *ApJS*, **160**, 149
 Toomre A., 1964, *ApJ*, **139**, 1217
 Tremaine S., Weinberg M. D., 1984, *ApJ*, **282**, L5
 van Albada T. S., Bahcall J. N., Begeman K., Sancisi R., 1985, *ApJ*, **295**, 305
 van der Kruit P. C., Searle L., 1981, *A&A*, **95**, 105
 Villa-Vargas J., Shlosman I., Heller C., 2010, *ApJ*, **719**, 1470
 Weinberg M. D., 1985, *MNRAS*, **213**, 451
 Widrow L. M., Pym B., Dubinski J., 2008, *ApJ*, **679**, 1239
 Young J. E., Kuzio de Naray R., Wang S. X., 2015, *MNRAS*, **452**, 2973
 Zwaan M. A., van der Hulst J. M., de Blok W. J. G., McGaugh S. S., 1995, *MNRAS*, **273**, L35

This paper has been typeset from a $\text{\TeX}/\text{\LaTeX}$ file prepared by the author.